

The development of an implicit full f method for electromagnetic particle simulations of Alfvén waves and energetic particle physics

Z. X. Lu,¹ G. Meng,¹ M. Hoelzl,¹ and Ph. Lauber¹
Max-Planck-Institut für Plasmaphysik, 85748 Garching, Germany

In this work, an implicit scheme for particle-in-cell/Fourier electromagnetic simulations is developed and applied to studies of Alfvén waves in one dimension and in tokamak plasmas. An analytical treatment is introduced to achieve efficient convergence of the iterative solution of the implicit field-particle system. Its application to the one-dimensional uniform plasma demonstrates its applicability in a broad range of β/m_e values. The toroidicity induced Alfvén eigenmode (TAE) is simulated using the widely studied case defined by the ITPA Energetic particle (EP) Topical Group. The real frequency and the growth (or damping) rate of the TAE with (or without) EPs agree with previous results reasonably well. The full f electromagnetic particle scheme established in this work provides a possible natural choice for EP transport studies where large profile variation needs to be captured in kinetic simulations.

I. INTRODUCTION

The gyrokinetic particle-in-cell (PIC) simulation serves as a first-principle-based tool for the studies of tokamak plasmas¹, and has revealed the importance of the zonal flow², the kinetic properties of energetic particles³ and the edge transport features⁴. While most gyrokinetic particle codes are based on the explicit method and the δf method⁵, implicit PIC in slab geometry has been reported featured with good properties such as energy and momentum conservation and the capability of allowing large time steps⁶. In addition, the full f method does not rely on the separation of the equilibrium and the perturbation and thus allows to handle massive changes of the profiles in the course of a simulation⁷. In the study of MHD/fluid problems, the mixed explicit-implicit scheme has been developed⁸, which shed some light on the development of gyrokinetic or hybrid particle-fluid method (kinetic MHD). One crucial issue in both fluid problem and kinetic problem is to treat the parallel dynamics accurately, considering the distinct features in parallel and perpendicular direction such as the large parallel to perpendicular transport coefficients ratio and, when kinetic particles are included, the fast response of electrons in the parallel direction⁹. While the pullback scheme is developed successfully for the electromagnetic simulation, the implicit scheme shows comparable linear properties and thus, similar efficiency/accuracy, compared to the those of the pullback scheme, using a numerical dispersion relation valid in slab geometry¹⁰. Moreover, the implicit scheme is expected to bring in good conservation properties and time step advantages^{6,11}. The applications of the implicit scheme in the simulation of the electrostatic toroidal ion temperature gradient instability has been reported¹² and a fully implicit scheme is explored recently in the particle simulation code XGC¹³. Nevertheless, the development and the application of the implicit full f scheme on the study of Alfvén modes and energetic particle (EP) physics in tokamak plasmas have not been reported.

In this work, an implicit scheme for particle simulations is developed and implemented in TRIMEG-

GKX. Instead of solving the implicit field-particle system numerically¹³, we developed the analytical expansion for solving the implicit solution in order to generate the linear system, whose solution converges to that of the non-linear system. This scheme is applied to the study of the one dimensional Shear Alfvén Wave (SAW) and the Toroidicity induced Alfvén Eigenmode (TAE) excited by the energetic particles. This work aims at providing

1. a demonstration of the applicability of the implicit method for the study of the SAW in tokamak plasmas;
2. a mixed implicit-explicit scheme for particle simulations, with analytical simplifications, as a practical way to upgrade the TRIMEG code¹⁴, meanwhile also as a potential solution for JOREK and other existing codes^{4,15,16}, for dealing with full f electromagnetic simulations;
3. a full f numerical tool for the study of Alfvén wave and energetic particle physics¹⁷ that can deal with strong profile changes and is complementing existing codes^{3,15,18}.

This paper is organized as follows. In Section II, the model for the electromagnetic particle simulation is introduced. In Section III, the implicit scheme with analytical treatment is derived. In Section IV, the simulation results of SAW in slab geometry and the TAE in tokamak plasmas are shown. In Section V, we provide summary and outlook.

II. ELECTROMAGNETIC MODEL

In this section, the electromagnetic model is presented. In order to understand the performance and the applicability of this implicit scheme with analytical treatment, we introduce the equations for the electromagnetic simulations in general geometry and its reduction to one dimension. Furthermore, the normalization and the mixed particle-in-cell-particle-in-Fourier (PIC-PIF) scheme are introduced.

For the tokamak geometry, the coordinates (r, ϕ, θ) are adopted and the magnetic field is represented as $\mathbf{B} = \nabla\psi \times \nabla\phi + F\nabla\phi$. An ad hoc equilibrium has been adopted, featured with concentric circular magnetic flux surfaces and constant F . Nevertheless, the scheme in this work is general, and it can be readily extended to arbitrary tokamak geometry.

A. Gyrokinetic Vlasov-Poisson equations and the parallel electron dynamics

The gyrokinetic Poisson-Ampère system is described as follows,

$$-\nabla_{\perp} \cdot \sum_s \frac{n_{0s} e_s}{\omega_c B} \nabla_{\perp} \delta\phi = \sum_s e_s \delta n_s , \quad (1)$$

$$-\nabla_{\perp}^2 \delta A_{\parallel} = \mu_0 \sum_s \delta j_{\parallel, s} , \quad (2)$$

where $\omega_c = e_s B / m_s$, the subscript ‘ s ’ and ‘ \parallel ’ indicate the species ‘ s ’ and the component parallel to the equilibrium magnetic field respectively, and μ_0 is the vacuum permeability.

The guiding center’s equations of motion are as follows,

$$\frac{d}{dt} \dot{\mathbf{R}} = \mathbf{v}_{\parallel} + \mathbf{v}_d + \delta \mathbf{v} , \quad (3)$$

$$\frac{d}{dt} v_{\parallel} = \dot{v}_{\parallel 0} + \delta \dot{v}_{\parallel} , \quad (4)$$

$$\mathbf{v}_d = \frac{m_s}{e_s B^2} \left(v_{\parallel}^2 + \mu B \right) \mathbf{b} \times \nabla B , \quad (5)$$

$$\delta \mathbf{v} = \frac{\mathbf{b}}{B} \times \nabla (\delta\phi - v_{\parallel} \delta A_{\parallel}) , \quad (6)$$

$$\dot{v}_{\parallel 0} = -\mu \partial_{\parallel} B , \quad (7)$$

$$\delta \dot{v}_{\parallel} = -\frac{e_s}{m_s} (\partial_{\parallel} \delta\phi + \partial_t \delta A) , \quad (8)$$

where the magnetic moment $\mu = v_{\perp}^2 / (2B)$, v_{\perp} is the perpendicular velocity, $\mathbf{b} = \mathbf{B} / B$. In order to minimize the technical complexity of the code implementation and to focus on the implicit scheme and the physics, we have ignored the finite Larmor radius effect and the higher order terms $\sim \rho_s / L_B$, compared with the more comprehensive gyrokinetic model^{2,4,9}, where $\rho_s = v_{\perp} / \omega_c$ is the Larmor radius of the particle species ‘ s ’, and L_B is the characteristic length of the equilibrium magnetic field. In spite of the simplification, it can be shown that the energy $E = v^2 / 2$ and the canonical toroidal angular momentum $P_{\phi} = e_s \psi + m v_{\parallel} F / B$ are conserved for the guiding center motion in equilibrium, i.e.,

$$\frac{d}{dt} E_0 = 0 , \quad \frac{d}{dt} P_{\phi 0} = 0 , \quad (9)$$

where the subscript ‘0’ indicates the variables in equilibrium magnetic field.

For the one dimensional (1D) case, we consider the guiding center motion in uniform magnetic field ($\mathbf{v}_d = 0$, $\dot{v}_{\parallel 0} = 0$). In addition, we assume uniform density and

temperature, and thus the term $\mathbf{b} \times \nabla (\delta\phi - v \delta A_{\parallel})$ is eliminated in the linear dispersion relation since $(\partial_t + v_{\parallel} \partial_{\parallel} + \delta \dot{v}_{\parallel} \partial / \partial v_{\parallel}) \delta f = -\delta \mathbf{v} \cdot \nabla f_0 - \delta \dot{v}_{\parallel} \partial_{\parallel} f_0 = -\delta \dot{v}_{\parallel} \partial_{\parallel} f_0$, where $f = f_0 + \delta f$, f_0 and δf are the equilibrium and the perturbed distribution functions respectively. Equations 3 – 8 for the guiding center are reduced to

$$\frac{dl}{dt} = v_{\parallel} , \quad (10)$$

$$\frac{dv_{\parallel}}{dt} = -\frac{e_s}{m_s} (\partial_{\parallel} \delta\phi + \partial_t \delta A_{\parallel}) , \quad (11)$$

where l is the coordinate along the magnetic field. This 1D model is a good test case for the implicit scheme, since the most numerically challenging term $\partial_t \delta A_{\parallel}$ is retained. The numerical scheme that applies to this 1D model can be readily extended for the tokamak geometry, for treating the $\partial_t \delta A_{\parallel}$ term.

B. Normalization

The normalization units of the length and the time are $R_N = 1 m$, $t_N = R_N / v_N$, where $v_N = \sqrt{2T_N / m_N}$, m_N is the proton mass, T_N is the reference temperature, chosen to be the on-axis ion temperature in this work. Other variables are normalized using v_N , $t_N \dots$, i.e., $v_{\parallel} = \bar{v}_{\parallel} v_N$, $R = \bar{R} R_N$. In the following, for the sake of simplicity, the bar $\bar{\cdot}$ is omitted when no confusion is introduced.

The normalized field equations are as follows,

$$-\nabla_{\perp} \cdot g \nabla_{\perp} \delta\phi = C_P \delta N , \quad (12)$$

$$-\nabla_{\perp}^2 \delta A_{\parallel} = C_A \delta J , \quad (13)$$

$$g = \sum_s M_s \frac{n_{0s} B_0^2}{\langle n \rangle B^2} , \quad \delta N = \sum_s e_s \frac{\delta n_s}{\langle n \rangle} , \quad \delta J_{\parallel} = \sum_s \frac{\delta j_{\parallel, s}}{\langle n \rangle} ,$$

where $C_P = 1 / \rho_N^2$, $C_A = \beta / \rho_N^2$, $\rho_N = m_N v_N / (e_N B_0)$, B_0 in this work is chosen as the on-axis magnetic field, $\beta = 2\mu_0 \langle n \rangle T_N / B_0^2$ and $\langle n \rangle$ is the volume averaged density.

The normalized equations of motion for the guiding center are expressed as follows,

$$\mathbf{v}_d = \frac{M_s B_0}{e_s B^2} \rho_N \left(v_{\parallel}^2 + \mu B \right) \mathbf{b} \times \nabla B , \quad (14)$$

$$\delta \mathbf{v} = \frac{B_0}{B} \rho_N \mathbf{b} \times \nabla (\delta\phi - v_{\parallel} \delta A_{\parallel}) , \quad (15)$$

$$\dot{v}_{\parallel 0} = -\mu \partial_{\parallel} B , \quad (16)$$

$$\delta \dot{v}_{\parallel} = -\frac{\bar{e}_s}{M_s} (\partial_{\parallel} \delta\phi + \partial_t \delta A) , \quad (17)$$

where $M_s = m_s / m_N$, $\bar{e}_s = e_s / e_N$. The Poisson equation, the Ampère’s law and the guiding center’s equations of motion in (r, θ, ϕ) coordinates can be readily obtained (Appendix A).

C. The mixed PIC-PIF scheme using finite element and Fourier basis function

The field variables are decomposed using Fourier basis function in (θ, ϕ) directions and using finite elements in r direction,

$$\delta\phi(r, \phi, \theta) = \sum_{n,m,k} \delta\phi_{nmk} \Lambda_k(r) e^{in\phi+im\theta} , \quad (18)$$

$$\delta A_{\parallel}(r, \phi, \theta) = \sum_{n,m,k} \delta A_{\parallel,nmk} \Lambda_k(r) e^{in\phi+im\theta} , \quad (19)$$

where n and m are the toroidal and poloidal harmonic numbers and k serves as the radial index. In the full f scheme, the physics distribution function is represented by the markers,

$$f(\mathbf{R}, v_{\parallel}, \mu) = \frac{N_{ph}}{N_{ptot}} \sum_p \frac{w_p}{2\pi B_{\parallel}^*} \delta(\mathbf{R} - \mathbf{R}_p) \delta(v_{\parallel} - v_{\parallel,p}) \delta(\mu - \mu_p) , \quad (20)$$

where N_{ptot} is the marker number, N_{ph} is the physical particle number, w_p is set according to the initial physical and the marker distributions, $2\pi B_{\parallel}^*$ is the Jacobian of the guiding center coordinates. The quasi-neutrality equation and the Ampère's law are converted to the weak form,

$$\bar{M}_{A,nmjk} \cdot \delta\phi_{nmk} = C_P \delta N_{nm}^k , \quad (21)$$

$$\bar{M}_{P,nmjk} \cdot \delta A_{\parallel,nmk} = C_A \delta J_{nm}^k , \quad (22)$$

$$\bar{M}_{P,nmjk} = \int_{r_0}^{r_1} dr \Lambda_j \nabla_{\perp,nm} \cdot g \nabla_{\perp,nm} \Lambda_k , \quad (23)$$

$$\bar{M}_{A,nmjk} = \int_{r_0}^{r_1} dr \Lambda_j \nabla_{\perp,nm} \cdot \nabla_{\perp,nm} \Lambda_k , \quad (24)$$

$$\delta N_{nm}^k = C_{p2g} \sum_p \frac{R_0}{rR} w_p e^{-i(n\phi_p+m\theta_p)} , \quad (25)$$

$$\delta J_{nm}^k = C_{p2g} \sum_p \frac{R_0}{rR} w_p v_{\parallel,p} e^{-i(n\phi_p+m\theta_p)} , \quad (26)$$

where $\nabla_{\perp,nm}$ is the Fourier representation of ∇_{\perp} with ∂_{θ} and ∂_{ϕ} replaced with im and in respectively, $C_{p2g} = (r_1^2 - r_0^2)/(2N_{ptot})$, and when calculating $\bar{M}_{A,nmjk}$ and $\bar{M}_{P,nmjk}$ in the code, we made use of the integration by parts. Note that δN_{nm}^k and δJ_{nm}^k are different from δN_{nmk} and δJ_{nmk} defined by

$$\delta N(r, \phi, \theta) = \sum_{n,m,k} \delta N_{nmk} \Lambda_k(r) e^{in\phi+im\theta} , \quad (27)$$

$$\delta J(r, \phi, \theta) = \sum_{n,m,k} \delta J_{nmk} \Lambda_k(r) e^{in\phi+im\theta} , \quad (28)$$

III. IMPLICIT SCHEME WITH ANALYTICAL TREATMENT

In this section, for the sake of simplicity, we use the 1D problem to demonstrate the procedure of the implicit scheme and the analytical treatment. The key issue is to mitigate the numerical instability in the direction parallel to the magnetic field, originating from $\partial_t \delta A_{\parallel}$ in the equation of motion, especially when the value of $\beta/(M_e k_{\perp}^2)$ is large. The implicit scheme for the 3D geometry can be readily done with the same procedure.

A. Shear Alfvén wave in uniform slab geometry

In the minimum model of SAW, the ion response is described with the polarization density, and only one kinetic species (electron) is kept. Omitting the subscript $s = e$, the normalized equations are

$$\frac{dl}{dt} = v_{\parallel} , \quad (29)$$

$$\frac{dv_{\parallel}}{dt} = \frac{1}{M_e} (\partial_{\parallel} \delta\phi + \partial_t \delta A_{\parallel}) , \quad (30)$$

$$\nabla_{\perp}^2 \delta\phi = C_P \delta N , \quad (31)$$

$$\nabla_{\perp}^2 \delta A_{\parallel} = C_A \delta J_{\parallel} . \quad (32)$$

The Fourier component of the density and current are obtained using particle-in-Fourier in the parallel direction,

$$\delta N_{k_l} = \frac{1}{N_{ptot}} \sum_p e^{-ik_l l_p} , \quad (33)$$

$$\delta J_{k_l} = \frac{1}{N_{ptot}} \sum_p v_{\parallel} e^{-ik_l l_p} , \quad (34)$$

where Fourier decomposition is applied to the field and moment variables, e.g, $\delta N(l) = \sum_k \delta N_k \exp\{ikl\}$, and k_l is the wave number along l .

The energy conservation is tested for this 1D model in Section IV A. Using Eq. 39, we have

$$E_{tot}(t) = E_{tot}(t + \Delta t) , \quad (35)$$

$$E_{tot}(t) \equiv E_{kin}(t) + E_B(t) + E_E(t) , \quad (36)$$

$$E_E = \frac{k_{\perp}^2}{2C_P} |\delta\phi_k(t)|^2 , E_B = \frac{k_{\perp}^2}{2C_A} |\delta A_k(t)|^2 , \quad (37)$$

where $E_{kin}(t)$ is the particle kinetic energy.

B. The implicit scheme for the particle-field system

The implicit scheme is realized by applying the iteration scheme to the particle-field system. The purpose of the iteration between the particle pusher and the field

solver is to achieve the implicit solution to the Crank-Nicolson scheme, i.e.,

$$\frac{l^{t+\Delta t} - l^t}{\Delta t} = \frac{v_{\parallel}^{t+\Delta t} + v_{\parallel}^t}{2}, \quad (38)$$

$$\frac{v_{\parallel}^{t+\Delta t} - v_{\parallel}^t}{\Delta t} = \frac{1}{2M_e} \partial_{\parallel} [\delta\phi^{t+\Delta t} + \delta\phi^t] + \frac{1}{M_e} \frac{\delta A_{\parallel}^{t+\Delta t} - \delta A_{\parallel}^t}{\Delta t}, \quad (39)$$

$$\nabla_{\perp}^2 \delta\phi^{t,t+\Delta t} = C_P \delta N^{t,t+\Delta t}, \quad (40)$$

$$\nabla_{\perp}^2 \delta A_{\parallel}^{t,t+\Delta t} = C_A \delta J_{\parallel}^{t,t+\Delta t}, \quad (41)$$

In solving the equations of motion for particles, i.e., Eqs. 38 and 39, with the constraint $\Delta t v_{\parallel} k_{\parallel} \ll 1$, it is applicable to take Taylor expansion of Eqs. 38 and 39, which leads to the analytic expression as follows,

$$\begin{aligned} \frac{\Delta l}{\Delta t} &= \frac{1}{h} \left\{ v_{\parallel}^t + \frac{\Delta t}{4M_e} \partial_l [\delta\phi^{t+\Delta t}(l^t) + \delta\phi^t(l^t)] \right. \\ &\quad \left. + \frac{1}{2M_e} [\delta A^{t+\Delta t}(l^t) - \delta A^t(l^t)] \right\} \end{aligned} \quad (42)$$

$$\begin{aligned} \frac{\Delta v_{\parallel}}{\Delta t} &= \frac{1}{2M_e h} \left\{ \partial_l [\delta\phi^{t+\Delta t}(l^t) + \delta\phi^t(l^t)] + v_{\parallel}^t \Delta t \partial_l^2 \delta\phi^{t+\Delta t}(l^t) \right. \\ &\quad \left. + 2 \frac{\delta A^{t+\Delta t}(l^t) - \delta A^t(l^t)}{\Delta t} + 2v^t \partial_l \delta A^{t+\Delta t}(l^t) \right\} \cdot \left\{ \begin{array}{l} \delta\phi(t+\Delta t) \\ \delta A(t+\Delta t) \end{array} \right\}^{start,i+1} = \left\{ \begin{array}{l} \delta\phi(t+\Delta t) \\ \delta A(t+\Delta t) \end{array} \right\}^{start,i} + \left\{ \begin{array}{l} \Delta\delta\phi \\ \Delta\delta A \end{array} \right\}, \end{aligned} \quad (43)$$

A more rigorous way is to solve the nonlinear equations, i.e., Eqs 38 and 39, numerically, in order to achieve a good accuracy. In this work, Eqs. 38 and 39 are solved by first defining the residual as follows,

$$R_1 \equiv x^{t+\Delta t} - x^t - \frac{\Delta t}{2} [v_{\parallel}^{t+\Delta t} + v_{\parallel}^t], \quad (44)$$

$$\begin{aligned} R_2 &\equiv v^{t+\Delta t} - v^t - \frac{\Delta t}{2M_e} \partial_l [\delta\phi^{t+\Delta t}(l^{t+\Delta t}) + \delta\phi^t(l^t)] \\ &\quad - \frac{1}{M_e} [\delta A^{t+\Delta t} - \delta A^t], \end{aligned} \quad (45)$$

and iterating $(l^{t+\Delta t}, v^{t+\Delta t})$ to reach $R_1 \rightarrow 0, R_2 \rightarrow 0$. This can be achieved by solving $\Delta l, \Delta v$ as follows,

$$\bar{M}_R \cdot \begin{bmatrix} \Delta l \\ \Delta v \end{bmatrix} = - \begin{bmatrix} R_1 \\ R_2 \end{bmatrix}, \quad \bar{M}_R = \begin{bmatrix} \frac{\partial R_1}{\partial l^{t+\Delta t}}, & \frac{\partial R_1}{\partial v^{t+\Delta t}} \\ \frac{\partial R_2}{\partial l^{t+\Delta t}}, & \frac{\partial R_2}{\partial v^{t+\Delta t}} \end{bmatrix}, \quad (46)$$

and by modifying (l, v) using $(\Delta l, \Delta v)$ in the next particle iteration with the given $\delta\phi, \delta A_{\parallel}$. In practice, Eqs. 42 and 43 can serve as the initial condition of the rigorous calculation of particle's implicit solution, namely Eqs. 44 – 46.

The main steps for iterations are as follows (all variables are at $t + \Delta t$ in the workflow, i.e., $\delta\phi = \delta\phi(t + \Delta t)$ etc),

$$\begin{aligned} &\xrightarrow{1} \left\{ \begin{array}{l} \delta\phi^{start} \\ \delta A_{\parallel}^{start} \end{array} \right\}^i \xrightarrow{2} \left\{ \begin{array}{l} l \\ v_{\parallel} \end{array} \right\}^i \xrightarrow{3} \left\{ \begin{array}{l} \delta N^{end} \\ \delta J^{end} \end{array} \right\}^i \\ &\xrightarrow{3} \left\{ \begin{array}{l} \delta\phi^{end} \\ \delta A_{\parallel}^{end} \end{array} \right\}^i \xrightarrow{4} \left\{ \begin{array}{l} \delta\phi^{start} \\ \delta A_{\parallel}^{start} \end{array} \right\}^{i+1} \end{aligned} \quad (47)$$

1. Each iteration starts with the given field $\{\delta\phi, \delta A\}^{start}(t + \Delta t)$. In each step from t to $t + \Delta t$, as the first iteration ($i = 1$), the explicit solution is used as the input of the first iteration. Namely, at time t , particles are pushed from $\{l(t), v_{\parallel}(t)\}$ to $\{l(t + \Delta t), v_{\parallel}(t + \Delta t)\}$ using $\partial_{\parallel} \delta\phi(t)$ and $(\delta A_{\parallel}(t) - \delta A_{\parallel}(t - \Delta t))/\Delta t$. Then $\{\delta\phi(t + \Delta t), \delta A_{\parallel}(t + \Delta t)\}$ are calculated using $\{l(t + \Delta t), v_{\parallel}(t + \Delta t)\}$ by solving the Poisson equation and the Ampère's law, and then serve as $\{\delta\phi^{start}, \delta A_{\parallel}^{start}\}_{i=1}$.
2. Particles are pushed from t to $t + \Delta t$ implicitly using $\{\delta\phi, \delta A\}^{start}(t + \Delta t)$ and $\{\delta\phi, \delta A\}(t)$ according to Eqs. 38 and 39, or, when $\Delta t v_{\parallel} k_{\parallel} \ll 1$, to Eqs. 42 and 43.
3. In the end of the iteration, $\{\delta\phi, \delta A\}^{end}(t + \Delta t)$ is calculated using Eqs. 40 and 41.
4. The field perturbation for the next iteration is set according to

where $\Delta\delta\phi$ and $\Delta\delta A_{\parallel}$ are determined in such a way that in the $(i + 1)$ th iteration,

$$\left\{ \begin{array}{l} \delta N^{start}(t + \Delta t) \\ \delta J^{start}(t + \Delta t) \end{array} \right\}^{i+1} = \left\{ \begin{array}{l} \delta N^{end}(t + \Delta t) \\ \delta J^{end}(t + \Delta t) \end{array} \right\}^{i+1}, \quad (48)$$

or, at least, convergence occurs with respect to i .

Applying the Taylor expansion on the left hand side near $\{\delta\phi^{start}, \delta A_{\parallel}^{start}\}^i$, and the right hand side of Eq. 48 near $\{\delta N^{start}, \delta J^{start}\}^i$, we have

$$\left\{ \left[\begin{array}{cc} \frac{1}{C_P} \nabla_{\perp}^2 & 0 \\ 0 & \frac{1}{C_A} \nabla_{\perp}^2 \end{array} \right] - \bar{M}_c \right\} \cdot \begin{bmatrix} \Delta\delta\phi \\ \Delta\delta A \end{bmatrix} = \begin{bmatrix} \Delta\delta\tilde{N} \\ \Delta\delta\tilde{J} \end{bmatrix} \quad (49)$$

where $\Delta\delta\tilde{N} \equiv \delta N^{end} - \delta N^{start}$, $\Delta\delta\tilde{J} \equiv \delta J^{end} - \delta J^{start}$,

$$\bar{M}_c \equiv \begin{bmatrix} \frac{\partial\delta N}{\partial\phi}, & \frac{\partial\delta N}{\partial A} \\ \frac{\partial\delta J}{\partial\phi}, & \frac{\partial\delta J}{\partial A} \end{bmatrix} = \begin{bmatrix} \frac{k_{\parallel}^2 (\Delta t)^2}{4M_e}, & -\frac{ik_{\parallel} \Delta t}{2M_e} \\ \frac{ik_{\parallel} \Delta t}{2M_e}, & \frac{1}{M_e} \end{bmatrix}. \quad (50)$$

In summary, Eqs. 38, 39 (or 42, 43), 40, 41, 49 and 50 embody our implicit scheme with analytical treatment and give the complete set for involving the system implicitly.

While the above implicit scheme is based on the 1D model, the implicit scheme in tomak plasmas can be implemented by applying either fully 3D implicit scheme on the same footing, or, as adopted in this work, the mixed implicit-explicit scheme. Using this mixed scheme, only the parallel equation of motion terms are treated implicitly but the other terms are treated using explicit scheme, such as Runge-Kutta method, as adopted in this work.

IV. NUMERICAL RESULTS

The one dimension SAW model is implemented in Matlab and the electromagnetic model for tokamak plasmas is implemented in Fortran. In this section, the simulation results are presented for these two cases. For the simulation in tokamak plasmas, the EP driven TAE case defined by the ITPA group is adopted¹⁹. LIGKA is run for the calculation of the TAE eigenvalue¹⁸, and for the comparison with the particle simulation results.

A. Shear Alfvén wave in 1D uniform plasma

As the benchmark of the particle simulation using the implicit scheme in 1D geometry (Eqs. 29–32), the electromagnetic dispersion relation in uniform plasma is adopted as the analytical solution,¹⁰

$$D = 1 - \frac{2\beta[1 + \bar{\omega}Z(\bar{\omega})]}{M_e(k_\perp \rho_{ti})^2} \left(\bar{\omega}^2 - \frac{M_e}{\beta} \right) = 0, \quad (51)$$

where k_\perp is the perpendicular wave number, Z is the plasma dispersion function, $\bar{\omega} = \omega/\omega_{te}$, $\omega_{te} = v_{te}k_\parallel$.

The simulation parameters are as follows. $k_\perp \rho_N = 0.2$, β/M_e is chosen in the range of [1/16, 32] in the parameter scan, which covers the typical regime of tokamak plasmas, e.g., $\beta = 1\%$, $M_e = 1/1836$, i.e., $\beta/M_e = 18.36$. The roots of the SAW are calculated in the complex space, by solving Eq. 51. The least damped roots with $\bar{\omega} = \pm 0.319 - 0.0017428i$ ($\beta/M_e = 10$) correspond to the SAW and serves as the analytical solution for the comparison with our particle simulation, while the other heavily damped roots can be hardly observed in the particle simulations.

The particle simulation based on the implicit scheme shows its performance in SAW studies, as shown in Fig. 2. In this case, the marker number $N_{ptot} = 10^5$, the time step $dt = 0.01 \cdot T_{SAW}$, where the SAW period $T_{SAW} = 2\pi/(v_A k_\parallel)$, $\beta/M_e = 4$. The total particle kinetic energy and the wave energy are calculated as shown on the first row. As the wave gets damped, the total particle kinetic energy grows. In the second line, the δB component (magenta line) and the δE component (blue line) oscillate with the same amplitude, but with 90 degrees of phase shift. The total energy (blue line in the first row) indicates good conservation properties. The relative error of the total energy is shown in the third row demonstrating that $[E(t) - \bar{E}]/\bar{E}$ stays in a low level around $5 \cdot 10^{-3}$, where \bar{E} is the time average of $E(t)$.

The real frequency and the damping rate of the SAW calculated using the implicit particle code and the eigenvalue solver (Eq. 51) are shown in Fig. 3. The marker number is 10^6 . For the weakly damped SAW (e.g., $\beta/M_e = 16$), the frequency ω_r and the damping rate γ are fitted in $10 \cdot T_{SAW}$, while for the SAW with larger damping rate (e.g., $\beta/M_e = 1/2$), ω_r and γ are fitted in

$4 \cdot T_{SAW}$. The maximum time step size used in the scan is $dt = T_{SAW}/20$ for $\beta/M_e = 1/16$ and the minimum one is $dt = T_{SAW}/120$ for $\beta/M_e = 32$. The small and large β/M_e limits correspond to the electrostatic limit and the small $|E_\parallel|/|\partial_\parallel \delta \phi|$ limit, respectively. The implicit scheme shows its capability in the small electron mass condition, which is usually a challenge in kinetic particle simulations, due to the quick electron response to the E_\parallel . The scan with fixed β (but varying m_e) and that with fixed m_e (but varying β) show no difference in the mode eigenvalue, which is obvious from the dependence of the analytical dispersion relation Eq. 51 on β/M_e .

B. Toroidicity induced Alfvén eigenmode damping and excitation

To simulate the Alfvén modes in tokamak plasmas, Eqs 12–17 are solved using the implicit particle scheme. The TAE is simulated using the parameters of the widely studied ITPA case¹⁹. The major radius $R_0 = 10 m$, minor radius $a = 1 m$, on-axis magnetic field $B_0 = 3 T$, the safety factor profile $q(r) = 1.71 + 0.16r^2$. The electron density is constant with $n_{e0} = 2.0 \cdot 10^{19} m^{-3}$, $T_e = 1 keV$. The EP density profile is

$$n_f(r) = n_{f0} c_3 \exp\left(-\frac{c_2}{c_1} \tanh \frac{r - c_0}{c_2}\right), \quad (52)$$

where $n_{f0} = 1.44131 \cdot 10^{17} m^{-3}$, the subscript ‘ f ’ indicates EPs (fast particles), $c_0 = 0.49123$, $c_1 = 0.298228$, $c_2 = 0.198739$, $c_3 = 0.521298$. The EP temperature is $400 keV$. Since the dominant ion response is already included in the polarization density in the Poisson equation, no kinetic ions are included in this work.

1. Numerical verification

The field solver is tested using the Method of Manufactured Solutions (MMS), without including particles. The Poisson solver and the Ampère solver are both constructed from the mass and stiffness matrices, corresponding to ∂_r^2 , ∂_r and $f(r)$, where $f(r)$ is a function of r . As a result, testing the Ampère solver is sufficient for the numerical verification of the basic field operators. The Ampère’s law can be written as (Eq. A1)

$$\left(\frac{\partial^2}{\partial r^2} + \frac{1}{r} \frac{\partial}{\partial r} - \frac{m^2}{r^2}\right) \delta A_{\parallel, m} = C_A \delta J_m, \quad (53)$$

where the toroidal mode number n is omitted since $n = -6$ is chosen. The analytical solution is given as

$$\begin{aligned} \delta A_{\parallel, m, ana} &= c_0 + c_1 r + a_J J_m(r) + e^{-\left(\frac{r-r_c}{W}\right)^2}, \quad (54) \\ C_A \delta J_{m, ana} &= a_2 r^2 + a_3 r^3 + a_+ r^m + a_- r^{-m} - a_J J_m(r) \\ &+ e^{-\left(\frac{r-r_c}{W}\right)^2} \times \left[\frac{4(r-r_c)^2}{W^4} - \frac{2}{W^2} - \frac{2(r-r_c)}{rW^2} - \frac{m^2}{r^2} \right], \quad (55) \end{aligned}$$

The right hand side of the Ampère's law is set to Eq. 55 in the Ampère solver and the numerical solution $\delta A_{\parallel,m,num}$ is compared with $\delta A_{\parallel,m,ana}$ in Eq. 54. The relative error in the numerical solution $\sqrt{[\sum_k (f_{num,k} - f_{ana}(r_k))^2] / \sum_k f_{ana}^2(r_k)}$, where k indicates the radial grid index, $f = \delta A_{\parallel,m}$, is shown in Fig. 4, where N_r is the radial grid number. Reasonable convergence of the field solver is observed. In our simulation, by choosing $N_r = 60$, the relative error in δA_{\parallel} for given δJ is at the level of 10^{-3} in the field solver.

The particle pusher is tested by the diagnosis of the particle trajectory and the two constants of motion, namely, the energy E and the canonical toroidal momentum P_ϕ . The particle temperature is 400 keV. For passing particles (the upper row), $\mu = 0.04v_{ts}^2$, $v_{\parallel} \in [-2v_{ts}, 2v_{ts}]$ at $r = 0.5$, $\theta = 0$. For trapped particles (the lower row), $\mu \in [0.15v_{ts}^2, v_{ts}^2]$, $v_{\parallel} = -0.2v_{ts}$ at $r = 0.8$, $\theta = 0$. The particle trajectories are shown in Fig. 5, and the corresponding relative error in E and P_ϕ are $\sim 10^{-14}$ and lower, close to the precision of double-precision floating-point numbers ($\approx 1.11 \times 10^{16}$) adopted in the simulation.

In order to test the convergence of the implicit field-particle solver, the relative correction in $\delta\phi$ and δA_{\parallel} in every iteration are analyzed. In the iteration procedure Eq. 47, the iteration can be ended when $Err(\delta\phi) \equiv \sqrt{\sum(\Delta\delta\phi)^2 / \sum\delta\phi^2}$ and $Err(\delta A_{\parallel}) \equiv \sqrt{\sum(\Delta\delta A_{\parallel})^2 / \sum\delta A_{\parallel}^2}$ are small enough (typically, 10^{-8}). The convergence of the particle-field implicit solver in a typical simulation is shown in Fig. 6. Two time slices are selected for the diagnosis of the convergence. In 15 iterations, the relative error in $\delta\phi$ and δA_{\parallel} decreases to 10^{-8} and lower, as a good indication of convergence.

2. Toroidicity induced Alfvén eigenmode w/o EPs

The TAE is simulated with no EPs applied firstly. Two cases of the TAE damping are studied. In the first case, we choose $m_i/m_e = 200$, since this is the parameter used in the EP driven TAE in the next section and previous ORB5 simulations²⁰. In the second case, we choose $m_i/m_e = 1836$, in order to compare with the previous results where $m_i/m_e = 1836$ is used for the calculation of the TAE damping¹⁹. LIGKA is run for both cases as the benchmark. The initial density perturbation is loaded by initializing markers' displacement. The initial density perturbation has a Gaussian shape $p(r) = \sigma_p \exp\{-(r - r_{pc})^2 / W_p^2\}$. Since the noise level in density is estimated as $\sigma_{noise} = 1/\sqrt{N_{ptot}/N_r}$, the amplitude of the initial density perturbation is set to at least 2 times of σ , i.e., $\sigma_p = 2\sigma_{noise}$ in order to simulate the TAE mode structure and the time evolution clearly. The Gaussian shape $\exp\{-(r - r_{pc})^2 / W_p^2\}$ of the density perturbation is set to be as close as possible to the TAE eigenmode. In practice, we adopted $W_p = 0.025$, $r_{pc}(m = 10) = 0.47$, $r_{pc}(m = 11) = 0.51$.

The marker number is $N_{ptot} = 16 \cdot 10^6$, the time step size is $dt = T_{TAE}/100$ for $m_i/m_e = 200$ and $dt = T_{TAE}/800$ for $m_i/m_e = 1836$. The simulation completes 10 T_{TAE} on 8 computing nodes within around 10 hours for the $m_i/m_e = 200$ case and 12.5 T_{TAE} within around 80 hours, with each node containing two Intel Xeon Gold 6148 processors (Skylake (SKL), 20 cores @ 2.4 GHz).

The time evolution of the TAE for $m_i/m_e = 200$ is shown in the top left frame of Fig. 7. The physics value of the electrostatic potential perturbation, $\delta\phi_c$, is measured at $r = 0.5, \theta = 0$. The time evolution is clear, indicating the proper simulation of the TAE. The analytical TAE frequency $\omega_{TAE} = v_A/(2qR_0) = 417.8 \cdot 10^3 \text{rad/s}$ is used as the reference. The real frequency fitted during $t/T_{TAE} \in [1, 10]$ gives the real frequency $\omega_r/\omega_{TAE} = 0.9615$, i.e., $\omega_r = 401.7 \cdot 10^3 \text{rad/s}$. The damping rate from the simulation is $\gamma/\omega_{TAE} = -0.011999$, i.e., $\gamma = -5013/s$. The mode frequency and the damping rate are compared with the results from LIGKA¹⁸. In LIGKA, the eigenvalue is calculated using the integral along the unperturbed particle orbit numerically. The value from this LIGKA numerical model $\gamma/\omega_r = -1.293\%$ is close to the TRIMEG-GKX result $\gamma/\omega_r = -1.248\%$. For the $m_i/m_e = 1836$ case, the frequency and the damping rate are $(\omega_r, \gamma) = (0.98142, -0.004907) \cdot \omega_{TAE}$ by using the wave energy E_E defined in Eq. 37 during $t/T_{TAE} \in [5, 12.5]$, in order to enhance the signal for this weakly damped mode. The value from LIGKA $\gamma/\omega_r = -0.5008\%$ is close to the TRIMEG-GKX result $\gamma/\omega_r = -0.5000\%$ for the realistic electron mass ratio. In the previous benchmark results¹⁹, using the realistic electron mass, the damping rate is $-1103/s$ for GYGLES, $-567/s$ (co propagating TAE) or -1705 (counter propagating TAE) for EUTERPE. In recent ORB5 simulation, the damping rate is $1825/s \sim 2190/s$ (Fig. 6 of Ref. [21]). In our simulation, both co- and counter-propagating TAEs are included and the estimated damping $\gamma = 2050/s$ is also comparable to other codes.

The 2D TAE mode structures are shown in the top middle and top right columns of Fig. 7. The mode width is consistent with previous simulation results with full width at half maximum $\Delta r \approx 0.06$ in the mode envelope. The magnitude of the $m = 10$ poloidal harmonic is larger than those of other harmonics, which is consistent with the observations by other codes such as LIGKA, GYGLES, ORB5 and EUTERPE¹⁹.

3. Energetic particle driven Toroidicity induced Alfvén eigenmode

For the EP driven TAE, the marker numbers for electrons and EPs are $N_{ptot,e} = 128 \cdot 10^6$, $N_{ptot,f} = 32 \cdot 10^6$, and the time step size is $dt = T_{TAE}/100$. The simulation completes on 24 computing nodes within around 36 hours. The time evolution of the EP driven TAE is shown in the bottom left frame of Fig. 7. Since the initial perturbation is not rigorously resembling the eigenmode

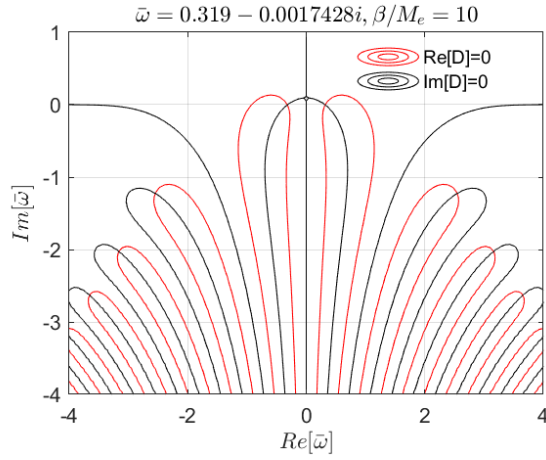


FIG. 1. The roots of the dispersion relation. The red or the black lines indicate the real or the imaginary parts of the SAW dispersion relation, Eq. 51, and their intersection gives the eigenmode solution $D(\bar{\omega}) = 0$. The least damped root with maximum $|Im(\zeta)|$ corresponds to the SAW.

with EP effects taken into account, it's damped firstly during $0 < t/T_{TAE} < 2$ and then the TAE is excited by EPs. The real frequency fitted during $t/T_{TAE} \in [4, 10]$ is $\omega_r/\omega_{TAE} = 0.9276$. The growth rate fitted during the growing phase ($2.5 < t/T_{TAE} < 5.5$) gives $\gamma/\omega_{TAE} = 0.090806$ (most codes give $\gamma/\omega_{TAE} \approx 9\% \sim 12\%$ ¹⁹).

The 2D mode structure and the radial profile of the poloidal harmonics at $t/T_{TAE} = 5.5$ are shown in the bottom middle and bottom right of Fig. 7. The broadening of the radial envelope (full width at half maximum ~ 0.12 from the bottom right frame) is larger by 100% than that of the TAE damping case in the top right frame. This is due to the EPs' non-perturbative effects broadening the mode structure^{3,20}. Another feature is the mode structure symmetry breaking, namely, the mode structure distortion, due to the EPs' contribution to the non-Hermitian part of the dispersion relation²²⁻²⁴. More quantitative studies on the properties of the mode structure symmetry breaking using this full f simulation and its effects on the EP transport²⁵, will be performed in future work.

V. SUMMARY AND OUTLOOK

In this work, an implicit full f scheme has been developed for the electromagnetic particle simulation of the damping and the excitation of Alfvén modes. This work provides a potential method for EP transport simulations which is able to maintain the kinetic effects of all particles and the electromagnetic effect. The main techniques have been developed as follows.

1. An analytical treatment has been derived for obtaining the implicit solution of the field-particle system, by linearizing the nonlinear implicit particle-

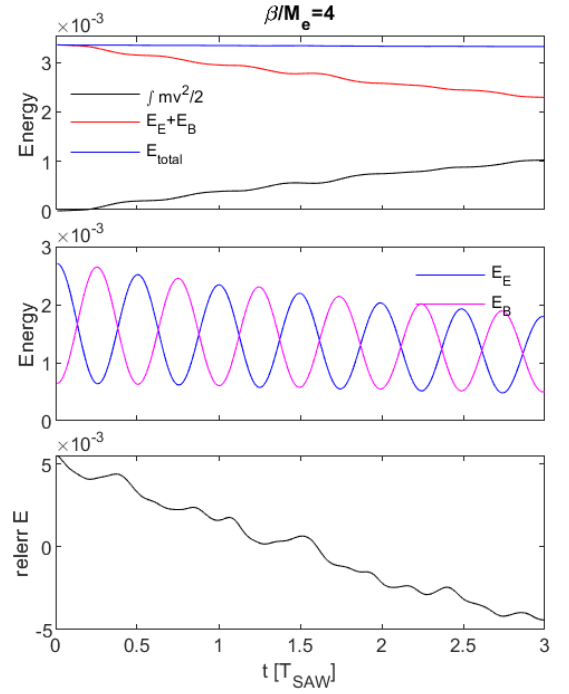


FIG. 2. Top: time evolution of the particle kinetic energy (black line), wave energy (red) and the total energy (blue); middle: the wave energy E_E and E_B defined by Eq. 37; bottom: relative error of total energy, defined as $(E(t) - \bar{E})/\bar{E}$, where \bar{E} is the time average value.

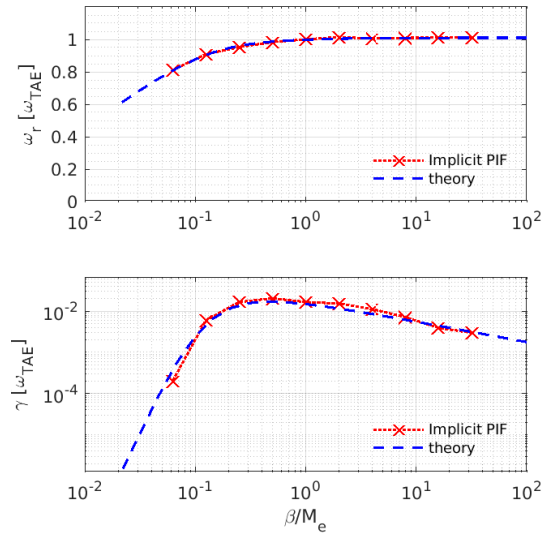


FIG. 3. The theoretical value solved from Eq. 51 (blue broken lines) and the simulation results using the implicit particle method (crosses) of the real frequency (top) and the damping rate (bottom) of the SAW.

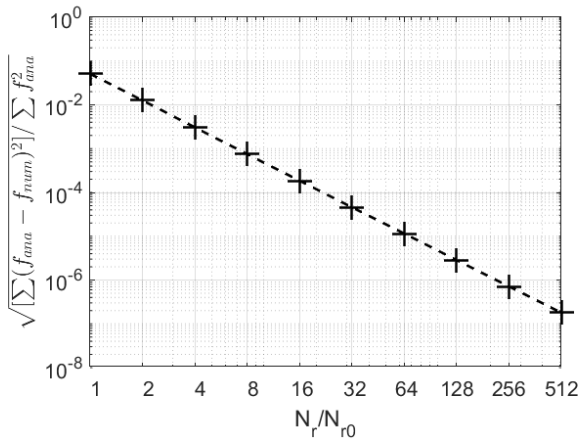


FIG. 4. The relative error in the solution to the Ampère's law versus different radial grid numbers using the Method of Manufactured Solutions, i.e., Eqs. 55 and 54, where $N_{r0} = 10$.

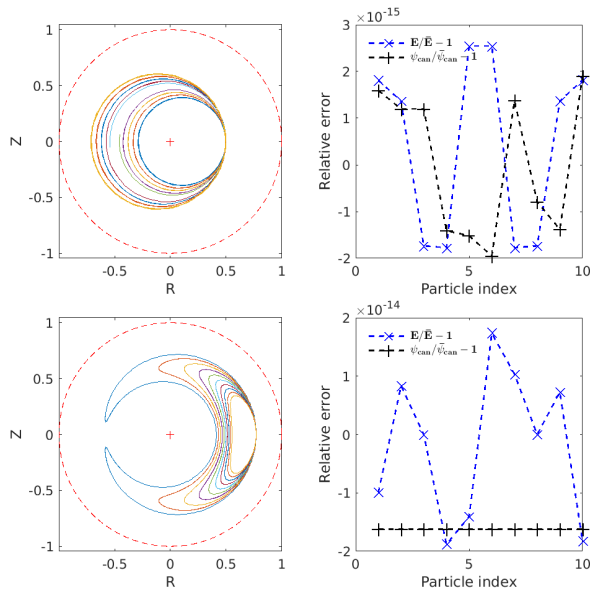


FIG. 5. The guiding center trajectories and relative error of energy and toroidal canonical momentum for passing particles (the first row) and trapped particles (the second row). The relative error in E and P_ϕ is $\sim 10^{-14}$ or lower, close to the precision of the double-precision floating-point number used in the simulation ($\approx 1.11 \times 10^{-16}$).

field system, which gives a practical way to solve the nonlinear system, as shown in Eqs. 38, 39, 40, 41, 49 and 50.

2. The mixed implicit-explicit scheme is developed to simulate the TAE by implicitly treating the parallel motion, which is usually the most challenging when the particle mass is small, but treating the other parts explicitly.

The implicit scheme in this work shows the following performance in the study of Alfvén waves and EP physics.

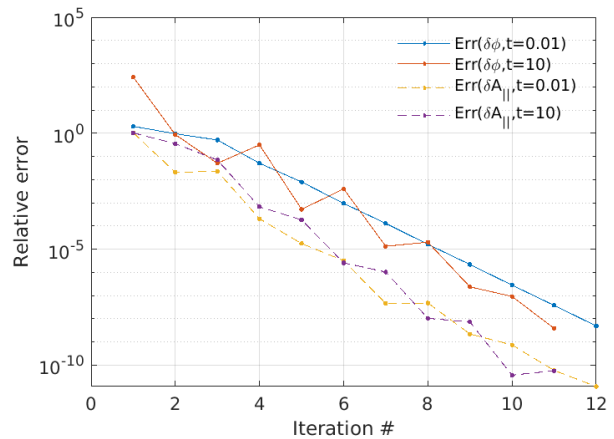


FIG. 6. The convergence of $\delta\phi$ (lines) and δA_{\parallel} (dashed lines) at the beginning ($t = 0.01T_{TAE}$) and the end ($t = 10T_{TAE}$) of EP driven TAE case in Section IV B 3.

1. Using the analytical derivation based implicit scheme, good convergence of the field-particle solver is demonstrated (Fig. 4).
2. By applying to the 1D shear Alfvén wave problem, this implicit scheme shows good energy conservation and capabilities of calculating the frequency and damping rate properly in a broad range of β/M_e values, including the small electron mass condition (Fig. 3).
3. The application of this method to the TAE problem shows its applicability for electromagnetic simulations with/without EPs (Fig. 7). The TAE mode structure distortion due to the non-perturbative effects of the EPs is observed, consistent with previous simulations^{3,20} and theoretical studies^{22–24}.

More dedicated studies related to the numerical performance of this implicit full f scheme for the electromagnetic physics will be addressed in future, and physics problems such as the mode structure symmetry breaking and EP transport will be studied. The application of this method to the whole plasma volume study using unstructured meshes¹⁴ or structured Bezier basis functions¹⁶, is expected to enable more comprehensive studies of the global electromagnetic kinetic effects and edge physics.

ACKNOWLEDGMENTS

Simulations in this work were performed on Max Planck Computing & Data Facility (MPCDF). Discussions with and inputs from G. Huysmans, K. Kormann, A. Mishchenko, A. Bottino, T. Hayward-Schneider, B. Sturdevant and F. Zonca are appreciated by ZL. This work is supported by the EUROfusion Enabling Research Projects WP19-ER/ENEA-05 and WP19-ER/MPG-03. This work has been carried out within the framework of

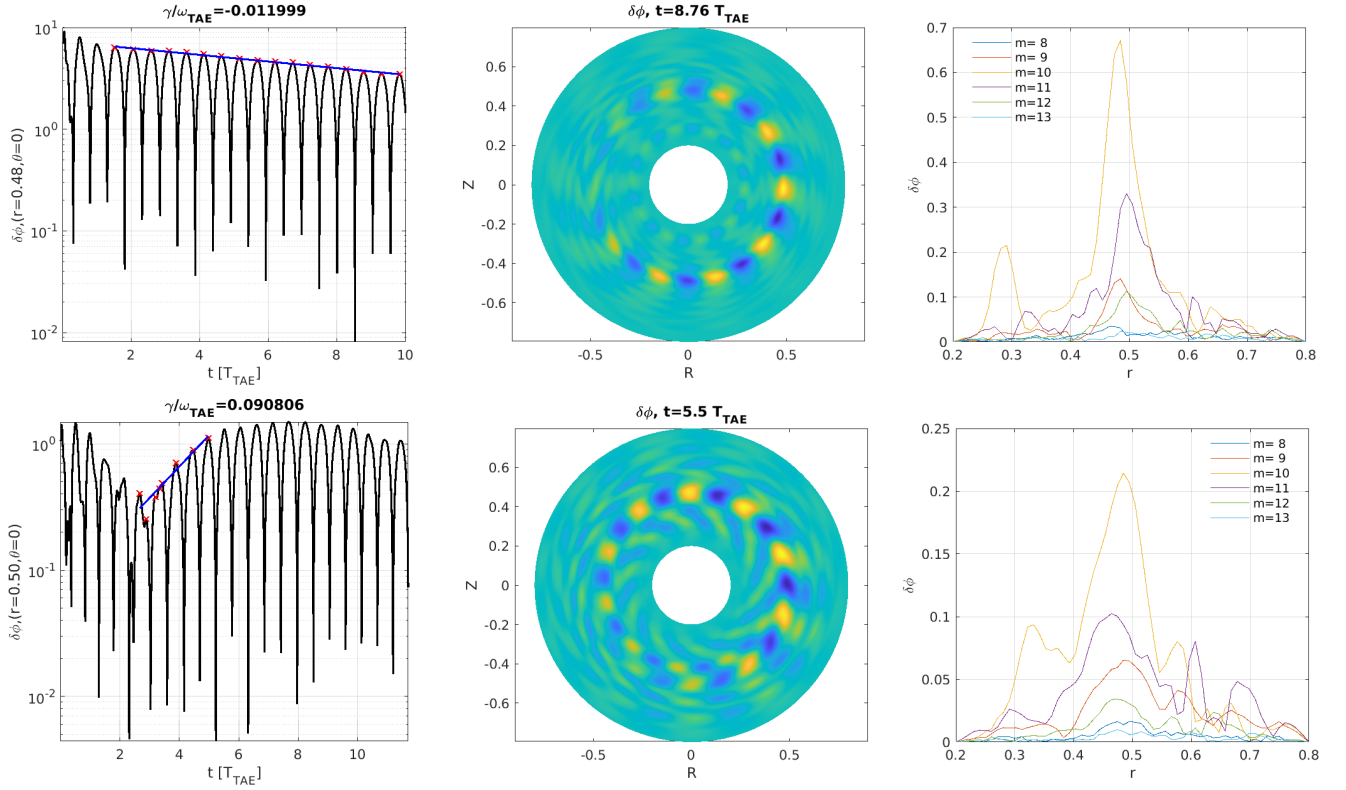


FIG. 7. The first row: TAE damping w/o EPs; the second row: TAE driven by EPs. Left: the time evolution of the TAE. The blue line indicates the linear fit using the logarithmic amplitude peak values along t during the selected time period (red crosses). $\delta\phi(r_c, \theta = 0)$ is normalized using T_{e0}/e as adopted by other work²⁰. The 2D mode structure of the TAE $Re[\delta\phi]$ (middle column) and the radial structure of the different poloidal harmonics (right). The toroidal mode number $n = -6$, the electron to ion mass ratio $m_e/m_i = 1/200$ for both cases.

the EUROfusion Consortium and has received funding from the Euratom research and training programme 2014-2018 and 2019-2020 under grant agreement No 633053. The views and opinions expressed herein do not necessarily reflect those of the European Commission.

Appendix A: Field and guiding center equations in (r, θ, ϕ) coordinates

In (r, θ, ϕ) , the Ampère's law is written as

$$\left(L_{rr} - \frac{m^2}{r^2}\right) \delta A_{\parallel, m} = C_A \delta J_m, \quad (\text{A1})$$

$$L_{rr} \equiv \frac{\partial^2}{\partial r^2} + \frac{1}{r} \frac{\partial}{\partial r}, \quad (\text{A2})$$

where the perpendicular Laplacian operator has been approximated using that in (r, θ) plane, since $B_\theta/B_\phi = r/(qR) \ll 1$. For quasi-neutrality equation, the toroidal coupling is calculated using

$$g_s = g_{s0} \frac{B_0^2}{B^2} \approx g_{s0} [1 + 2\epsilon_c \cos \theta], \quad (\text{A3})$$

where $\epsilon_c = r/R_0$. The quasi-neutrality equation is expressed as

$$\begin{aligned} & \left(L_{rr} - \frac{m^2}{r^2}\right) \delta\phi_m + \epsilon_c g_0 \left[L_{rr} - \frac{m(m+1)}{r^2}\right] \delta\phi_{m+1} \\ & + \epsilon_c g_0 \left[L_{rr} - \frac{m(m-1)}{r^2}\right] \delta\phi_{m-1} = C_P \delta N_m, \end{aligned} \quad (\text{A4})$$

where $g_0 = \sum_s g_{s0}$.

For guiding center's equations of motion, in (r, ϕ, θ) coordinates, we have

$$\frac{d\bar{r}_d}{dt} = \frac{M_s B_0 \bar{\rho}_N}{\bar{e}_s B^3 R} \frac{F}{r} \partial_\theta B, \quad (\text{A5})$$

$$\frac{d\phi_d}{dt} = \frac{M_s B_0 \bar{\rho}_N}{\bar{e}_s B^3 R} \frac{\partial_r \psi}{R} \partial_r B, \quad (\text{A6})$$

$$\frac{d\theta_d}{dt} = \frac{M_s B_0 \bar{\rho}_N}{\bar{e}_s B^3 R} \frac{F}{r} \partial_r B, \quad (\text{A7})$$

$$\frac{d\delta\bar{r}}{dt} = \frac{B_0}{B} \bar{\rho}_N \left(\frac{b_\phi}{r} \partial_\theta \delta G - \frac{b_\theta}{R} \partial_\phi \delta G \right), \quad (\text{A8})$$

$$\frac{d\delta\phi}{dt} = \frac{B_0}{B} \bar{\rho}_N \frac{b_\theta}{R} \partial_r \delta G, \quad (\text{A9})$$

$$\frac{d\delta\theta}{dt} = -\frac{B_0}{B} \bar{\rho}_N \frac{b_\phi}{r} \partial_r \delta G, \quad (\text{A10})$$

$$\dot{v}_{\parallel 0} = -\frac{\bar{\mu}\partial_r\psi}{R^2}\sin\theta, \quad (\text{A11})$$

$$\delta\dot{v}_{\parallel} = -\frac{\bar{e}_s}{M_s}(\partial_{\parallel}\delta\bar{\phi} + \partial_t\delta\bar{A}), \quad (\text{A12})$$

where $\delta G = \delta\bar{\phi} - \bar{v}_{\parallel}\delta A_{\parallel}$.

- ¹W. Lee, *Phys. Fluids* **26**, 556 (1983).
²Z. Lin, T. S. Hahm, W. Lee, W. M. Tang, and R. B. White, *Science* **281**, 1835 (1998).
³Z. Wang, Z. Lin, I. Holod, W. Heidbrink, B. Tobias, M. Van Zeeland, M. Austin, *et al.*, *Phys. Rev. Lett.* **111**, 145003 (2013).
⁴C. Chang, S. Ku, G. Tynan, R. Hager, R. Churchill, I. Cziegler, M. Greenwald, A. Hubbard, and J. Hughes, *Phys. Rev. Lett.* **118**, 175001 (2017).
⁵S. Parker and W. Lee, *Phys. Fluids B* **5**, 77 (1993).
⁶G. Chen, L. Chacón, and D. C. Barnes, *J. Comput. Phys.* **230**, 7018 (2011).
⁷J. A. Heikkinen, S. J. Janhunen, T. P. Kiviniemi, and F. Ogando, *J. Comput. Phys.* **227**, 5582 (2008).
⁸S. Günter and K. Lackner, *J. Comput. Phys.* **228**, 282 (2009).
⁹A. Mishchenko, A. Bottino, A. Biancalani, R. Hatzky, T. Hayward-Schneider, N. Ohana, E. Lanti, S. Brunner, L. Villard, M. Borchardt, *et al.*, *Comput. Phys. Commun.* **238**, 194 (2019).
¹⁰R. Kleiber, R. Hatzky, A. Könies, A. Mishchenko, and E. Sonnendrücker, *Phys. Plasmas* **23**, 032501 (2016).
¹¹B. I. Cohen, A. B. Langdon, D. W. Hewett, and R. J. Procassini, *J. Comput. Phys.* **81**, 151 (1989).
¹²B. Sturdevant, Y. Chen, and S. Parker, *Phys. Plasmas* **24**, 081207 (2017).
¹³B. Sturdevant, S.-H. Ku, C. Chang, R. Hager, L. Chacon, and G. Chen, *Bulletin of the American Physical Society* (2019).
¹⁴Z. Lu, P. Lauber, T. Hayward-Schneider, A. Bottino, and M. Hoelzl, *Phys. Plasmas* **26**, 122503 (2019).
¹⁵E. Lanti, N. Ohana, N. Tronko, T. Hayward-Schneider, A. Bottino, B. McMillan, A. Mishchenko, A. Scheinberg, A. Biancalani, P. Angelino, *et al.*, *Comput. Phys. Commun.*, 107072 (2019).
¹⁶G. Huysmans and O. Czarny, *Nucl. Fusion* **47**, 659 (2007).
¹⁷L. Chen and F. Zonca, *Rev. Mod. Phys.* **88**, 015008 (2016).
¹⁸P. Lauber, S. Günter, A. Könies, and S. D. Pinches, *J. Comput. Phys.* **226**, 447 (2007).
¹⁹A. Könies, S. Briguglio, N. Gorelenkov, T. Fehér, M. Isaev, P. Lauber, A. Mishchenko, D. Spong, Y. Todo, W. Cooper, *et al.*, *Nucl. Fusion* **58**, 126027 (2018).
²⁰A. Biancalani, A. Bottino, M. Cole, C. Di Troia, P. Lauber, A. Mishchenko, B. Scott, and F. Zonca, *Plasma Phys. Controlled Fusion* **59**, 054004 (2017).
²¹F. Vannini, A. Biancalani, A. Bottino, T. Hayward-Schneider, P. Lauber, A. Mishchenko, I. Novikau, E. Poli, and A. U. Team, *Phys. Plasmas* **27**, 042501 (2020).
²²R. Ma, F. Zonca, and L. Chen, *Phys. Plasmas* **22**, 092501 (2015).
²³Z. Lu, X. Wang, P. Lauber, and F. Zonca, *Nucl. Fusion* **58**, 082021 (2018).
²⁴Z. Lu, X. Wang, P. Lauber, E. Fable, A. Bottino, W. Hornsby, T. Hayward-Schneider, F. Zonca, and C. Angioni, *Plasma Phys. Controlled Fusion* **61**, 044005 (2019).
²⁵G. Meng, P. Lauber, Z. Lu, and X. Wang, *Nucl. Fusion* **60**, 056017 (2020).